Second-Order Discretization in Space and Time for Radiation-Hydrodynamics

Simon Bolding[a], Joshua Hansel[a], Jarrod D. Edwards[b], Jim E. Morel[a], Robert B. Lowrie[c]

[a]*Department of Nuclear Engineering, 337 Zachry Engineering Center, TAMU 3133, Texas A&M University, College Station, Texas, 77843*
[b]*Phenomenology and Sensor Science Department, Sandia National Laboratory, Albuquerque, NM*
[c]*Computational Physics Group CCS-2, Los Alamos National Laboratory, P.O. Box 1663, MS D413, Los Alamos, NM 87545*

Abstract

Second-order accurate discretizations for radiation-hydrodynamics are currently an area of great interest. Second-order methods used to solve the hydrodynamics equations and second-order methods used to solve the radiation transport equation often differ fundamentally, making it difficult to combine them in a second-order manner. Here, we present a implicit-explicit (IMEX) method for solving the 1-D equations of radiation-hydrodynamics that is second-order accurate in space and time. Our radiation-hydrodynamics model consist of the 1-D Euler equations coupled with a grey radiation S_2 approximation. Our RH method combines the MUSCL-Hancock method for solving the Euler equations with the TR/BDF2 time integration scheme and the linear-discontinuous Galerkin finite-element spatial discretization scheme for the S_2 radiation equations. The MUSCL-Hancock method is commonly used for hydrodynamic calculations and the linear-discontinuous Galerkin scheme is the standard for the S_n equations of radiative transfer. While somewhat similar, these schemes vary fundamentally with respect to the treatment of spatial slopes. We address the challenges inherent to coupling these different numerical methods and demonstrate how these challenges can be overcome. Using the method of manufactured solutions, we show that the method is second-order accurate in space and time for both the equilibrium diffusion and streaming limit, and we show that the method is capable of computing radiative shock solutions accurately by comparing our results with semi-analytic solutions.

1. Introduction

Radiation hydrodynamics (RH) describes thermal radiation propagating through a fluid and the effects of the radiation on the properties of that fluid. Second-order accuracy in time for radiation-hydrodynamics calculations is currently an area of considerable interest. Though detailed work has been done for time integration of radiation diffusion and transport [1, 2, 3, 4, 5, 6, 7], and likewise for fluid dynamics [8], research in second-order methods that couple the two has only recently been carried out [9, 10, 11]. Because of the dramatically different time scales of radiation diffusion/transport and fluid advection, RH calculations are usually treated using an implicit-explicit (IMEX) scheme [9, 10, 11]. In such algorithms, the fluid advection component is treated explicitly, whereas the radiation transport and energy exchange terms are treated implicitly; these time discretizations are appropriate for the behavior and time scales of each physics.

Sekora and Stone developed a scheme for RH that uses second-order Godunov methods to achieve second-order accuracy in space and time. This scheme is entirely explicit so that the time step is limited by the more rapidly varying radiation time scale [12]. Sekora's method is intended for the relativistic regime characterized as $a_{s\infty}/c < 0.1$, where a_∞ denotes the speed of sound of the material and c denotes the speed of light. In this case, the fluid and radiation time-scales are not dramatically different, and therefore, the Courant limit time-step constraint is not overly restrictive. However, for the non-relativistic regime, i.e. $a_{s\infty}/c < .01$, bounding the time-step according to the radiation time-scale will force the time steps to be at least two orders of magnitude smaller than the fluid time-scale. Kadioglu has also developed a second-order accurate scheme for both low and high energy density RH problems [13, 14]. Accuracy is achieved by incorporating the explicit algorithm into the implicit iterations. While this provides a tight coupling between the explicit and implicit terms, it is computationally more expensive than standard IMEX schemes, since the explicit block is solved in each nonlinear iteration [13].

In this work, we derive, implement, and test a new IMEX scheme for solving the equations of radiation hydrodynamics that is second-order accurate

in both space and time. We consider a 1-D RH system that combines a 1-D slab model of compressible fluid dynamics with a grey radiation S_2 model, given by:

$$\frac{\partial \rho}{\partial t} + \frac{\partial}{\partial x}\left(\rho u\right) = 0 \,, \tag{1a}$$

$$\frac{\partial}{\partial t}\left(\rho u\right) + \frac{\partial}{\partial x}\left(\rho u^2\right) + \frac{\partial}{\partial x}\left(p\right) = \frac{\sigma_t}{c}F_{r,0} \,, \tag{1b}$$

$$\frac{\partial E}{\partial t} + \frac{\partial}{\partial x}\left[\left(E + p\right)u\right] = -\sigma_a c\left(aT^4 - E_r\right) + \frac{\sigma_t u}{c}F_{r,0} \,, \tag{1c}$$

$$\frac{1}{c}\frac{\partial \psi^+}{\partial t} + \frac{1}{\sqrt{3}}\frac{\partial \psi^+}{\partial x} + \sigma_t \psi^+ = \frac{\sigma_s}{4\pi}cE_r + \frac{\sigma_a}{4\pi}acT^4 - \frac{\sigma_t u}{4\pi c}F_{r,0} + \frac{\sigma_t}{\sqrt{3\pi}}Eu \,, \tag{1d}$$

$$\frac{1}{c}\frac{\partial \psi^-}{\partial t} - \frac{1}{\sqrt{3}}\frac{\partial \psi^-}{\partial x} + \sigma_t \psi^- = \frac{\sigma_s}{4\pi}cE_r + \frac{\sigma_a}{4\pi}acT^4 - \frac{\sigma_t u}{4\pi c}F_{r,0} - \frac{\sigma_t}{\sqrt{3\pi}}Eu \,, \tag{1e}$$

where ρ is the density, u is the velocity, $E = \frac{\rho u^2}{2} + \rho e$ is the total fluid energy density, e is the specific internal energy density, T is the fluid temperature, E_r is the radiation energy density,

$$E_r = \frac{2\pi}{c}\left(\psi^+ + \psi^-\right) \,, \tag{2}$$

F_r is the radiation energy flux,

$$F_r = \frac{2\pi}{\sqrt{3}}\left(\psi^+ - \psi^-\right) \tag{3}$$

and

$$F_{r,0} = F_r - \frac{4}{3}E_r u \tag{4}$$

is an approximation to the comoving-frame flux.

Note that if we multiply Eqs. ((1d)) and (1e) by 2π and sum them, we obtain the radiation energy equation:

$$\frac{\partial E_r}{\partial t} + \frac{\partial F_r}{\partial x} = \sigma_a c(aT^4 - E_r) - \frac{\sigma_t u}{c}F_{r,0} \,, \tag{5a}$$

and if we multiply Eq. (1d) by $\frac{2\pi}{c\sqrt{3}}$, multiply Eq. (1e) by $-\frac{2\pi}{c\sqrt{3}}$ and sum them, we get the radiation momentum equation:

$$\frac{1}{c^2}\frac{\partial F_r}{\partial t} + \frac{1}{3}\frac{\partial E_r}{\partial x} = -\frac{\sigma_t}{c}F_{r,0} \,. \tag{5b}$$

3

Note that Eqs. (5a) and (5b) are known as the P_1 radiation approximation and are completely equivalent to Eqs. (1d) and (1e) under a similarity transformation defined by the invertible mapping given by Eqs. (2) and (3).

Equations (1a) through (1e) are closed in our calculations by assuming an ideal equation of state (EOS):

$$p = \rho e(\gamma - 1),$$
(6a)

$$T = \frac{e}{C_v},$$
(6b)

where γ is the adiabatic index, and C_v is the specific heat. However, our method is compatible with any valid EOS.

Our RH method combines the MUSCL-Hancock method (MHM) for solving the Euler equations with the TR/BDF2 time discretization scheme and the linear-discontinuous Galerkin finite-element (LDGFEM) spatial discretization scheme for the S_2 equations. The MUSCL-Hancock method is commonly used for hydrodynamic calculations and the linear-discontinuous Galerkin scheme is the standard for the S_n radiation equations. While somewhat similar, these schemes vary fundamentally with respect to the treatment of spatial slopes. The resolution of conflicts arising from these disparate slope treatments is a major component of our new RH method.

One of the most common methods for discretizing the S_n equations in time is the Crank-Nicolson method, also known as the Trapezoid Rule. This is a well-known, implicit method that is second-order accurate; however, its principal drawback is that it can become highly oscillatory for stiff systems. An alternative to this is a linear-discontinuous Galerkin method in time. Despite the fact that this scheme is more accurate than the Crank-Nicolson method and damps oscillations quickly, it has a much higher computational cost that is roughly equivalent to that of solving two Crank-Nicolson systems simultaneously over each time step. In this work, we use the TR/BDF2 scheme for discretizing the radiation S_2 and energy exchange terms in time. The TR/BDF2 scheme is a one-step, two-stage[1] implicit method that was first derived in [15]. There is actually a family of such schemes, but one member of the family can be shown to be optimal in a certain sense. A simple version of this method that is near-optimal was applied to the equations of

---

[1]Here we use the term "stage" to refer to an implicit equation that must be solved within each time step in a discretization scheme.

radiative transfer in [16], where it is shown to be both L-stable, accurate, and efficient. In [16], the near-optimal TR/BDF2 scheme is used to solve the equations of radiative transfer. It consists of a Crank-Nicolson step over half the time step followed by a BDF2 step over the remainder of the time step. The TR/BDF2 method has a computational cost that is roughly equivalent to that of solving two Crank-Nicolson systems sequentially over each time step. Here we introduce an alternative form of the simple TR/BDF2 method that is particularly useful for our purposes.

A critical issue for radiation transport spatial discretizations is the preservation of the diffusion limit. Radiation-hydrodynamics problems often contain highly diffusive regions. In any type of calculation it is generally expected that accurate solutions will be obtained whenever the spatial variation of the solution is well-resolved by the mesh. However, use of a consistent transport discretization scheme in a highly diffusive problem will not guarantee such behavior. To ensure it, a consistent discretization scheme must "preserve" the diffusion limit or "be asymptotic preserving" [17]. A consistent discretization that does not preserve the diffusion limit will only yield accurate results in highly diffusive problems if the spatial cells are small with respect to a mean-free-path. Since the diffusion length can a arbitrarily large with respect to a mean-free-path, discretization schemes that are not asymptotic preserving can be prohibitively expensive to use in problems with highly diffusive regions due to the need to arbitrarily over-resolve the solution. Thus preservation of the radiation diffusion limit is an essential property of any radiation-hydrodynamics scheme. Although we only use an S_2 radiation treatment, our overall coupling and solution scheme is applicable to an S_n treatment of arbitrary order. The only caveat is that a higher order S_n model will require a standard iterative solution technique for the S_n equations themselves rather than directly solving those equations as we do. An important aspect of our study is that we are able to investigate preservation of the diffusion limit assuming an LDFEM spatial discretization for a S_2 treatment that will be valid for an S_n treatment of arbitrary order.

The MHM includes spatial differencing for the advection equations and incorporates a linear interpolation from cell-averaged values to compute the slopes. However, Lowrie and Morel show in [18] that interpolation schemes which only depend on the mesh geometry and do not incorporate additional physical data, e.g. cross-section values, fail to have the diffusion limit. Furthermore, the differences in spatial discretization between the advection and S_2 equations present considerable complications due to the fact that, in the

MHM, the slopes are determined from interpolations of the cell-centered unknowns; whereas, in the LDFEM, the slopes are computed as part of the solution to the discretized spatial moment equations. To add to these complications, the internal energy of the fluid represents an unknown in both the fluid advection and radiation equations. The easy solution to this problem is to recompute the internal energy and radiation slopes at the beginning of each time step using the MHM limiter. Doing this, we were able to show that our method maintained the diffusion limit in 1D and reproduced shock solutions accurately. However, standard 2D and 3D hydrodynamics limiters use a spatial representation that will not maintain the radiation diffusion limit [19]. In particular, a simple linear dependence for the solution is assumed but a bilinear (2D) or a trilinear dependence (3D) is required [20]. Thus, to overcome this limitation, the method we present here retains the slopes computed by the LDFEM from one time step to the next. We use reconstructed slopes as determined in the MUSCL-Hancock method only to compute the advection fluxes, and we use the retained LDFEM slopes to initialize the implicit calculations for the radiation energy density and flux and for the fluid temperature update. This allows our method to reduce to its standard constituent methods when the contributions from coupled physics are negligible, and we believe it will also allow us to preserve the diffusion limit in a future extension of our method to 2D and 3D. Of course, this remains to be demonstrated.

The remainder of this paper is structured as follows. In Section 2, we give an overview of our second-order accurate radiation-hydrodynamics method, and we give a detailed description in the Appendix. In Section 3, we use the method of manufactured solutions to show that our method is second-order accurate in both space and time in the equilibrium diffusion limit as well as in the streaming limit. Then, in Section 4, we demonstrate the capability of our method to accurately compute radiation-hydrodynamic shocks by reproducing semi-analytic shock solutions. Finally, in Section 5, we summarize our results and present our conclusions and recommendations for future work.

2. Overview of the Radiation-Hydrodynamics Method

There are two cycles per time step. The first cycle spans the first half of the time step and the second spans the second half. The first cycle proceeds as follows:

1. Do a standard MHM predictor step.

2. Enter an iteration loop

    (a) Update the fluid momentum using lagged radiation momentum deposition

    (b) Simultaneously solve the total energy equation and the S_2 equations for the new radiation intensities and updated fluid internal energies using an LDG discretization in space and a Backward Euler discretization in time.

    (c) Iterate until the fluid momenta, internal energies, and radiation intensities converge.

3. Do a standard MHM corrector step.

4. Initialize internal energy slopes to previous radiation solve values.

5. Enter an iteration loop

    (a) Update the fluid momentum using lagged radiation momentum deposition

    (b) Simultaneously solve the total energy equation and the S_2 equations for the new radiation intensities and updated fluid internal energies using an LDG discretization in space and a Crank-Nicolson discretization in time.

    (c) Iterate until the fluid momenta, internal energies, and radiation intensities converge.

The second cycle proceeds as follows:

1. Do a standard MHM predictor step.

2. Enter an iteration loop.

    (a) Update the fluid momentum using lagged radiation momentum deposition.

    (b) Simultaneously solve the total energy equation and the S_2 equations for the new radiation intensities and updated fluid internal energies using an LDG discretization in space and a Backward Euler discretization in time.

    (c) Iterate until fluid momenta, internal energies, and radiation intensities converge.

3. Do a standard MHM corrector step.

4. Initialize internal energy slopes to previous radiation solve values.

5. Enter an iteration loop

    (a) Update the fluid momentum using lagged radiation momentum deposition

(b) Simultaneously solve the total energy equation and the S_2 equations for the new radiation intensities and updated fluid internal energies using an LDG discretization in space and a BDF2 discretization in time.

(c) Continue iteration until fluid momenta, internal energies, and radiation intensities converge.

Note that the combination of Crank-Nicolson and BDF2 discretization results in a TR/BDF2 discretization over the full time step. We use a standard Backward Euler discretization for the radiation solves during the predictor stages, which only requires first-order accuracy. One advantage to applying the full MHM over each half time step is that, if the time step size is being determined by the Courant limit, we can take twice the usual time step. In this case, the cost of four radiation solves per time step per iteration is mitigated. Alternatively, this algorithm could be viewed as a mixed, two-stage algorithm with alternating Crank-Nicolson and BDF2 solves over time steps (from this viewpoint, the time step sizes are governed by the standard Courant limit and there is only two radiation solves per time step).

Our scheme is designed in such a way that, if the radiation contributions to the hydrodynamics are negligible, the standard MHM solution is obtained over each half time step, and if the hydrodynamics contributions to the radiation diffusion are negligible, the standard TR/BDF2 solution for radiative transfer is obtained over the full time step. The process of iterating between the radiation momentum deposition to the fluid and the nonlinear radiation/internal energy solves is necessary to conserve total momentum. The radiation momentum deposition is usually small in the high energy density laboratory physics regime, so a Picard-type iteration for the momentum deposition is adequate. In problems with stronger radiation momentum deposition, a better iteration scheme might be required.

The explicit hydrodynamic steps imposes a limit on the maximum time step size our algorithm can take. Using a standard estimate of numerical wave speeds [8], our time step size for the n-th time step is estimated as

$$\Delta t^n = 2 \, \mathrm{CFL} \max_i \left(|u_i| + |a_{i,s}| \right))$$ (7)

where CFL is a chosen parameter, Δt is the full time step, and u_i and $a_{i,s}$ are the fluid velocity and sound speed for each cell i.

2.1. Diffusion Limit

Of importance to obtaining the diffusion limit is using the correct initial internal energy slopes in the simultaneous solve for the S_2 intensities and the updated internal energies. Each MHM step provides slopes for the mass densities, the fluid momentum densities, and the fluid total energies. From the mass and fluid momentum slopes one can compute kinetic energy slopes. These slopes are used together with the fluid internal energy slopes determined from the previous-cycle radiation/internal energy solve to initialize the left and right fluid total energies. A detailed description of how we modify the internal energy slopes can be found in Appendix A.4.

2.2. Slope limiting

McClarren and Lowrie [21] investigated the impact of slope limiting on asymptotic-preserving methods for hyperbolic systems with stiff relaxation terms that reduce to a parabolic description when relaxation dominates. This work is relevant to our radiation-hydrodynamics method. They found that a slope limiter must not introduce discontinuities at cell edges if asymptotic preservation is to be maintained. The minmod limiter has this property and is thus not suitable for radiation-hydrodynamics in general. However, the double minmod and the "sawtooth-free" limiter introduced in [21] do not have this property. Here we use the double minmod limiter.

2.3. Alternate Form of TBDF2 Method

We have derived a non-standard form of the TR/BDF2 time differencing scheme to facilitate determining the form of radiation coupling terms in the hydrodynamics equations. Applying this difference scheme to

$$\frac{\partial f}{\partial t} = \mathbf{A}f(t) \tag{8}$$

we obtain

$$\frac{2\left(f^{n+1/2} - f^n\right)}{\Delta t} = \frac{1}{2}(\mathbf{A}f)^{n+1/2} + \frac{1}{2}(\mathbf{A}f)^n, \tag{9}$$

$$\frac{2\left(f^{n+1} - f^{n+1/2}\right)}{\Delta t} = \frac{2}{3}(\mathbf{A}f)^{n+1} + \frac{1}{6}(\mathbf{A}f)^{n+1/2} + \frac{1}{6}(\mathbf{A}f)^n. \tag{10}$$

Note that each of these expression represents a conservation statement over each half time step. The usual expression that Eq. (10) replaces is

$$\frac{3\left(f^{n+1} - f^{n+1/2}\right)}{\Delta t} - \frac{\left(f^{n+1/2} - f^n\right)}{\Delta t} = (\mathbf{A}f)^{n+1}, \tag{11}$$

which is clearly not a conservation statement. Equation (10) is derived from Eq. (9) and Eq. (11).

NEED TO DISCUSS BC FOR HYDRO AND PROBABLY RADIATION

3. Second-Order Accuracy for the Method of Manufactured Solutions

To demonstrate that our method is second-order accurate in space and time, we use the method of manufactured solutions (MMS). With MMS, we assume a functional form of the exact solution and derive extraneous sources for each equation that ensure the equations are satisfied analytically. We compare our numerical solution to the MMS problem to the exact solution as we refine the solution in space and time to examine to determine the order-accuracy of the algorithm. Two MMS problems, one for the streaming limit and one for the equilibrium diffusion limit, were taken from [22]. These solutions are composed of a combination of trigonometric functions with periodic boundary conditions. The sources were re-expressed in to account for our S_2 model versus the P_1 radiation model. Additionally, our algorithm was implemented in a dimensionalized code, whereas the test problems are nondimensional.

An extraneous source is added to each equation of Eq. (1) to test the MMS problems. The analytic, dimensionalized forms of sources are determined from the resulting equations using symbolic computations, based on the chosen functional solution. These sources are then included in the discretized equations by evaluating spatial moments of the sources with high-accuracy quadrature. We quantify the error between exact and numerical solutions using a relative L_2 norm of cell-averaged quantities, defined as

$$L_2^{\text{rel}}(u) = \sqrt{\sum_i^{N_x} \left(u_i - u_i^{\text{ex}}\right)^2 \Delta x_i} \Bigg/ \sqrt{\sum_i^{N_x} \left(u_i^{\text{ex}}\right)^2 \Delta x_i} \tag{12}$$

where u is the quantity of interest and u_i^{ex} is the analytic solution averaged over the i-th spatial cell.

3.1. Accuracy in the Diffusion Limit

We have converted the nondimensional solutions in [22] to be compatible with our dimensionalized code. The problems are prescribed with two non-

dimensional parameters

$$\mathbb{P} = \frac{aT_\infty^4}{\rho_\infty a_{s\infty}^2}, \quad \mathbb{C} = \frac{c}{a_{s\infty}},$$

(13)

where $a_{s\infty}$, T_∞, and ρ_∞ are the reference sound speed, material temperature, and density, respectively. There is not a unique mapping from the nondimensional solutions to a dimensional form. Thus, it is necessary to choose additional dimensional material parameters. We have chosen in our redimensionalization process to specify a reference material density that produces solutions with reasonable magnitudes. The values for cross sections, γ, $\mathbb{P}$, and $\mathbb{C}$ are taken from [22]. We then determine C_v and the remaining reference scalings from Eq. (13), Eq. (6a), and Eq. (6b). The non-dimensional solutions are redimensionalized by multiplying each variable by the appropriate reference scaling.

For the diffusion limit problem, the following dimensionalized solutions were prescribed for the hydrodynamic solution:

$$\rho = \rho_\infty \left(\sin(x - t) + 2 \right),$$

(14a)

$$u = a_{s\infty} \frac{M}{2} \left(\cos(x - t) + 2 \right),$$

(14b)

$$p = \rho_\infty a_{s\infty}^2 \alpha \left(\cos(x - t) + 2 \right),$$

(14c)

where α and M are constants. The factor $M/2$ was introduced to ensure that the material velocity is below the material sound speed. Using the perfect gas equation of state relations (Eq. (6b) and (6a)), an expression for material temperature T can be derived. The dimensionalized radiation energy density and flux are the following in the equilibrium diffusion limit:

$$E_r = aT^4,$$

(15a)

$$F_r = \frac{1}{3\sigma_t} \frac{\partial}{\partial x} acT^4 + \frac{4}{3} aT^4 u,$$

(15b)

Eqs. (2) and (3) are used to derive corresponding expressions for ψ^+ and ψ^- from the above expressions. Symbolic computations can then be used to derive the analytic MMS sources for each equation by substituting the solution into the left side of Eq. (1).

Following [22], we explore convergence of the solution as the cell optical thickness $\tau = \sigma\Delta x$ and $\mathbb{C}/\Delta x$ remain constant. This is to ensure that

11

the solution remains diffusive, which would expose inaccuracy in methods that do not preserve the diffusion limit. As in [22], we use $\sigma = 10^5 \frac{N_x}{20}$ (cm^{-1}) and $\mathbb{C} = 10^5 \frac{N_x}{20}$, where N_x is the number of spatial cells for each simulation. The remaining problem specifications are $\rho_\infty = 1$ g cm^{-3}, $\alpha = 0.5$, $M = 0.9$, $\mathbb{P} = 0.001$, and $\gamma = \frac{5}{3}$. It is noted that because of how we have dimensionalized the solutions, the magnitude of reference parameters, and thus the solution, must change as $\mathbb{C}$ is modified. However, since our error norm is defined relative to the solution norm, we observe the proper convergence order. The simulation end time is 2π sh (1 sh = 10^{-8} s). The Δt for the coarsest mesh spacing is chosen based on a Courant condition, given by Eq. (7), and CFL=0.6. This ensures stability of the MHM algorithm. We then uniformly refine in space and time for each following simulation to demonstrate convergence in the two variables. It is worth noting that our first time step size is chosen based on the Courant condition given in Eq. (7), which is based on material velocity speeds. This is a much larger and more physically reasonable time step size for an IMEX scheme than those in [22], which based the Courant condition on a non-dimensional speed of light. The relative, iterative convergence tolerance of each nonlinear implicit solve is 1.E-10 for all simulations.

Figures A.1 and A.2 depict the error convergence as a function of Δx and Δt for internal energy and momentum, respectively. As demonstrated, the algorithm is second-order accurate in space and time for the equilibrium diffusion limit problem. Although not plotted here, second-order convergence was verified for E_r, F_r, and the other conserved and primitive hydrodynamic unknowns.

3.2. Streaming Limit

The second MMS problem corresponds to the streaming limit, in which the radiation and hydrodynamics are weakly coupled. In this limit, radiation streaming dominates relatively small radiation absorption and re-emission terms. Here, we keep the re-emission term small by making the opacity relatively small so that the radiation is nearly transparent to the fluid. Also, because the radiation streams much faster than the fluid, this results in a solution in which the unknowns evolve at significantly different time scales. The functional form of the streaming solutions are

$$\rho = \rho_\infty \left(\sin(x - t) + 2 \right) , \tag{16a}$$

$$u = a_{s\infty} M \left(\cos(x - t) + 2 \right) , \tag{16b}$$

12

$$p = \rho_\infty a_{s\infty}^2 \alpha \left(\cos(x - t) + 2 \right), \tag{16c}$$

$$E_r = aT_\infty^4 \alpha \left(\cos(x - \mathbb{C}t) + 2 \right) \tag{16d}$$

$$F_r = acT_\infty^4 \alpha \left(\cos(x - \mathbb{C}t) + 2 \right) \tag{16e}$$

Here, was can see that the wave speed of the radiation energy density is faster than that of the hydrodynamic unknowns by a factor of $\mathbb{C}$. This solution is also defined to mimic an isothermal flow regime, in which the radiation varies rapidly enough that changes in the fluid temperature are suppressed. In this case, the exact solution for the fluid temperature is a constant.

All problem parameters are fixed and then the space and time discretizations are refined uniformly, for each simulation. The problem is fully defined with the parameters $\mathbb{C} = 100$, $\mathbb{P} = 0.1$, $\rho_{infty} = 1$ g cm^{-3}, $\gamma = 5/3$, $\sigma_a = \sigma_t = u$ cm^{-1}, $\alpha = 0.5$ and $M = 0.9$. The relatively high value of $\mathbb{P}$ and low value of $\mathbb{C}$ produce a more difficult problem to simulate, requiring convergence of the implicit solves. As before, the initial Δt is based on a CFL of 0.6. The simulation is performed until the initial radiation have advanced two periods, i.e., until $t = 4\pi/10$.

Figures A.3 and A.4 depict the error convergence as a function of Δx and Δt for internal energy and momentum, respectively. The convergence in the streaming limit is closer to 1.8 for the momentum variable. A finer time step size may be required to resolve the radiation unknowns more accurately than the Courant condition requires. The time step size may not yet be in the asymptotically converging region.

4. Results for Radiation-Hydrodynamic Shocks

Reproducing radiative shocks accurately, particularly in the optically thick regime, represents a challenging problem in the simulation of radiation hydrodynamics. A numerical scheme must be able to meet these challenges well. We will compare simulated steady state, radiative shocks to semi-analytical solutions [?]. The semianalytic solutions are based on a diffusion radiation model, which is equivalent to our S_2 radiation model at steady state. To reduce simulation times, we initialize the shocks with the analytic steady state solution projected onto the cell centered meshes and run the simulation until steady state is reached. At the boundary, we compute the fluxes using our standard Riemann solver, setting the hydrodynamic unknowns on the outside of the boundary equal to the far-stream conditions. Our algorithm will not be second-order globally due to the discontinuity at

the shock [**?**]. Thus, we are not interested in order-accuracy here but are ensuring our code produce accurate solutions.

We test our algorithm for two radiative shocks, similar to those presented in [23], which incorporate a variety of structural features. For both shocks, we set $\gamma = 5/3$, $c_v = 0.14472799784454$ Jks keV^{-1} g^{-1} (1 Jk= 10^9 J), and $\sigma_a = 577.35$ cm^{-1}. The problem specifications for the farstream pre and post-shock regions are provided in Table A.1. and Table **??** for the Mach 1.2 and Mach 3 shock, respectively. Results are generated with a CFL condition of 0.6 and $N_x = 500$ spatial cells.

First, we compute the Mach 1.2 shock, which has a hydrodynamic shock but no ISP. Fig. A.5 compare our results with the semi-analytic solutions for the fluid and radiation temperature. We see good agreement between the two. In this solution, we see a discontinuity in both the density and fluid temperature due to the hydrodynamic shock, and the maximum temperature is bounded by the far-downstream temperature, since there is no ISP to drive it further.

A Mach 3 shock is simulated that has both a hydrodynamic shock and an ISP. Fig. A.6 compares our numerical material and radiation temperature with the semi-analytic solutions. In each of these figures, we can see the effects of the hydrodynamic shock, causing a discontinuity in both the fluid density and temperature. We can also see the Zel'dovich spike, caused by the ISP embedded within the hydrodynamic shock, driving up the fluid temperature at the shock front. This spike leads to the relaxation region downstream as the fluid temperature and radiation temperature equilibrate. Here, we can see that our results still show very good agreement with the semi-analytic solution.

5. Conclusions and Future Work

We develop a new IMEX method for solving the equations of radiation-hydrodynamics that is second-order accurate in space and time. In addition to accuracy, we meet the goals outlined in Section 1: it reliably converges non-linearities, rapidly damps oscillations, incorporates modern algorithms used by the hydrodynamics and radiation transport communities, appears to have straightforward extensibility to a full radiation transport model, preserves the diffusion limit in 1D in such a way that it is expected to preserve this limit in 2D and 3D, accurately computes radiative shocks, and reduces to

fundamental algorithms when the effects of coupled physics are negligible. Thus, it represents a very useful alternative to existing methods.

In future work, we recommend extending our radiation solver to incorporate a radiation transport model. The structure of our radiation-hydrodynamics algorithm should make this extension straightforward. Since our algorithm only requires the angle-integrated radiation energy density and radiation current, the radiation solver may, in some sense, be treated as a black box module to compute these quantities. Of course, the angular intensities will need to be preserved across time steps. Momentum is already conserved by the chosen implicit statements. It may not be necessary to fully converge the nonlinear solves in the predictor steps, but this will be problem dependent.

References

[1] R. G. McClarren, T. M. Evans, R. B. Lowrie, J. D. Densmore, Semi-Implicit Time Integration for Pn Thermal Radiative Transfer, Journal of Computational Physics 196 (2004) 566–590.

[2] R. B. Lowrie, A Comparison of Implicit Time Integration Methods for Nonlinear Relaxation and Diffusion, Journal of Computational Physics 196 (2004) 566–590.

[3] D. A. Knoll, R. B. Lowrie, J. E. Morel, Numerical Analysis of Time Integration Errors for Nonequilibrium Radiation Diffusion, Journal of Computational Physics 226 (2007) 1332–1347.

[4] G. L. Olson, Second-Order Time Evolution of Pn Equations for Radiation Transport, Journal of Computational Physics 228 (2009) 3027–3083.

[5] T. S. Axelrod, P. F. Dubois, C. E. R. Jr., An Implicit Scheme for Calculating Time- and Fequency-Dependent Flux Limited Radiation Diffusion in One Dimension, Journal of Computational Physics 54 (1984) 205–220.

[6] J. M. Stone, D. Mihalas, Upwind Monotonic Interpolation Methods for the Solution of the Time Dependent Radiative Transfer Equation, Journal of Computational Physics 100 (1992) 402–408.

[7] P. N. Brown, D. E. Shumaker, C. S. Woodward, Fully Implicit Solution of Large-Scale Non-equilibrium Radiation Diffusion with High Order Time Integration, Journal of Computational Physics 204 (2005) 760–783.

[8] E. Toro, Riemann Solvers and Numerical Methods for Fluid Dynamics: A Practical Introduction, Springer, 1999.

[9] R. B. Lowrie, J. E. Morel, J. A. Hittinger, The Coupling of Radiation and Hydrodynamics, Astrophysics Journal 521 (1999) 432–450.

[10] J. W. Bates, D. A. Knoll, W. J. Rider, R. B. Lowrie, V. A. Mousseau, On Consistent Time-Integration Methods for Radiation Hydrodynamics in the Equilibrium Diffusion Limit: Low-Energy-Density Regime, Journal of Computational Physics 167 (2001) 99–130.

[11] W. Dai, P. R. Woodward, Numerical Simulations for Radiation Hydrodynamics. I. Diffusion Limit, Journal of Computational Physics 142 (1998) 182–207.

[12] M. Sekora, J. Stone, A Higher Order Godunov Method for Radiation Hydrodynamics: Radiation Subsystem, Communication in Applied and Computational Mathematics 4 (2009) 135–152.

[13] S. Y. Kadioglu, A Second Order Self-Consistent IMEX Method for Radiation Hydrodynamics, Journal of Computational Physics 229 (2010) 8313–8332.

[14] S. Y. Kadioglu, A Fully Second Order Implicit/Explicit Time Integration Technique for Hydrodynamics Plus Nonlinear Heat Conduction Problems, Journal of Computational Physics 9 (2010) 3237–3249.

[15] R. E. Bank, W. M. Coughran, Jr., W. Fichtner, E. H. Grosse, D. J. Rose, R. K. Smith, Transient Simulation of Silicon Devices and Circuits, IEEE Transactions on Computer-Aided Design of Integrated Circuits and Systems 4 (1985) 436–451.

[16] J. D. Edwards, J. E. Morel, Nonlinear Variants of the TR/BDF2 Method for Thermal Radiative Diffusion, Journal of Computational Physics 230 (2011) 1198–1214.

[17] E. W. Larsen, J. E. Morel, J. W. F. Miller, Asymptotic Solutions of Numerical Transport Problems in Optically Thick, Diffusive Regimes, Journal of Computational Physics 69 (1987) 283–324.

[18] R. B. Lowrie, J. E. Morel, Issues with High-Resolution Godunov Methods for Radiation Hydrodynamics, Journal of Quantitative Spectroscopy & Radiative Transfer 69 (2001) 475–489.

[19] Z. J. Wang, High-order Methods for the Euler and NavierStokes Equations on Unstructured Grids, Progress in Aerospace Science 43 (2007) 1–41.

[20] M. L. Adams, Discontinuous Finite Element Transport Solutions in Thick Diffusive Problems, Nuclear Science and Engineering 137 (2001) 298–333.

[21] R. G. McClarren, R. B. Lowrie, The Effects of Slope Limiting on Asymptotic Preserving Numerical Methods for Hyperbolic Conservation Laws, Journal of Computational Physics 227 (2008) 9711–9726.

[22] R. G. McClarren, R. B. Lowrie, Manufactured Solutions for the P1 Radiation-Hydrodynamics Equations, Journal of Quantitative Spectroscopy & Radiative Transfer 109 (2008) 2590–2602.

[23] R. B. Lowrie, J. D. Edwards, Radiative Shock Solutions with Grey Non-equilibrium Diffusion, Shock Waves 18 (2008) 129–143.

[24] J. Morel, T. Wareing, K. Smith, Linear-Discontinuous Spatial Differencing Scheme for S_n Radiative Transfer Calculations, Journal of Computational Physics 128 (1996) 445–462.

Appendix A. The Time-Discretized Equations

In this section, we detail each of the equations for the MHM and iterative radiation solves. The radiative transfer and hydrodynamic operators are treated independently via operator-splitting. Within the predictor and corrector stage of each cycle, there is an explicit hydrodynamic solve, followed by an associated implicit radiation solve. We will use a $*$ superscript to denote the intermediate operator-splitting states of variables resulting from the hydrodynamic steps.

Appendix A.1. Notation for Edge Values

Here, we define our notation to differentiate between interior-edge unknowns and true face unknowns. Within a cell, interior-edge unknowns are used to represent a linear solution, wheras true face values are needed in integration of spatial derivatives. For example, the Riemann solver used in corrector steps produces a true face value for the flux, where as the predictor step uses interior-edge unknowns to estimate the flux within a cell. For the radiation balance equations, the interior-edge unknowns are used to define face unknowns depending on direction of travel.

Appendix A.2. The MUSCL-Hancock Method

The MHM handles the fluid advection portion of the RH equations by advancing the homogeneous Euler equations in time. The homogeneous Euler equations may be expressed in conservative form as

$$\frac{\partial \mathbf{H}}{\partial t} + \nabla \cdot \mathbf{F}(\mathbf{H}) = \mathbf{0} \,, \tag{A.1}$$

where $\mathbf{H}$ is a vector of the conservative unknowns and $\mathbf{F}(\mathbf{H})$ is the flux associated with each, i.e.,

$$\mathbf{H} = \begin{bmatrix} \rho \\ \rho u \\ E \end{bmatrix} \,, \qquad \mathbf{F}(\mathbf{H}) = \begin{bmatrix} \rho u \\ \rho u^2 + p \\ (E + p)u \end{bmatrix} \,. \tag{A.2}$$

Each cycle consists of a MHM predictor and corrector stage. For example, the first predictor step advances the hydrodynamic unknowns from H^n to $H^{*n+1/4}$. The predictor step begins by constructing a cell-wise linear representation of the solution using reconstructed slopes Δ_i^n:

$$\Delta_i^n = \frac{1}{2} \left(\Delta \mathbf{H}_{i-\frac{1}{2}}^n + \Delta \mathbf{H}_{i+\frac{1}{2}}^n \right) \,, \tag{A.3}$$

18

$$\Delta \mathbf{H}^n_{i-\frac{1}{2}} = \mathbf{H}^n_i - \mathbf{H}^n_{i-1}\,, \quad \Delta \mathbf{H}^n_{i+\frac{1}{2}} = \mathbf{H}^n_{i+1} - \mathbf{H}^n_i\,, \tag{A.4}$$

The slopes are modified using a double-minmod slope limiter to ensure positivity and stability [21]. A linear representation of the solution within each cell is then constructed as

$$\mathbf{H}^n_{i,L} = \mathbf{H}^n_i - \frac{\Delta^n_i}{2}\,, \quad \mathbf{H}^n_{i,R} = \mathbf{H}^n_i + \frac{\Delta^n_i}{2}\,, \tag{A.5}$$

This representation is then evolved by a quarter of a time step:

$$\mathbf{H}^{*n+\frac{1}{4}}_i = \mathbf{H}^n_i - \frac{\frac{1}{4}\Delta t}{\Delta x} \left(\mathbf{F}(\mathbf{H}^n_{i,R}) - \mathbf{F}(\mathbf{H}^n_{i,L}) \right)\,. \tag{A.6}$$

At this point, an implicit Euler radiation solve advances the system from $t^{*n+\frac{1}{4}}$ to $t^{n+\frac{1}{4}}$, as detailed in Sec. **??**. Then, the corrector step of the MUSCL-Hancock method is applied. The corrector step employs an approximate Riemann solver to compute the fluxes based on the predicted hydrodynamic variables, i.e.,

$$\mathbf{H}^{*n+\frac{1}{2}}_i = \mathbf{H}^n_i - \frac{2\Delta t}{\Delta x} \left(\mathbf{F}^{n+\frac{1}{4}}_{i+\frac{1}{2}} - \mathbf{F}^{n+\frac{1}{4}}_{i-\frac{1}{2}} \right)\,, \tag{A.7}$$

where the fluxes are computed using an HLLC approximate Riemann solver [8]. At each edge, the Riemann solver uses linearly extrapolated values, based on lagged hydrodynamic slopes. For example, at the edge $x_{i-\frac{1}{2}}$, the Riemann solver computes fluxes with the states $\mathbf{H}^{n+1/4}_i - \frac{\Delta^n_i}{2}$ and $\mathbf{H}^{n+\frac{1}{4}}_{i-1} + \frac{\Delta^n_{i-1}}{2}$. At a boundary, the Riemann solver uses either a specified far-stream state or a predicted state from the previous stage for periodic boundary conditions. For instance, at the edge $x_{1/2}$ the two states are $\mathbf{H}^{n+1/4}_1 - \frac{\Delta^n_1}{2}$ and $\mathbf{H}^{n+\frac{1}{4}}_N + \frac{\Delta^n_N}{2}$, for periodic boundary conditions.

Appendix A.3. The Iterative Radiation Solves

During each implicit radiation solve, the momentum deposition due to radiation and the energy exchange due to black-body emission must be iteratively solved. An outer fixed-point iteration is performed for the velocity update. Within each outer iteration, an analytic Newton step is taken for the radiative transfer terms. The iterations are repeated until convergence. The equations below are for the $k + 1$-st iteration within each stage of the algorithm.

Appendix A.3.1. Momentum Update Equation

During the iteration loop, a lagged estimates of the radiation unknowns are used to compute a new material momentum and velocity. The discretization of the radiation equations produces a linear solution within a cell, which is represented with edge unknowns, e.g., $E_{rL,i}$ and $E_{rR,i}$. The edge values for radiation momentum deposition are spatially averaged to update the cell-averaged material velocity. The BDF2 discretization of the velocity update equation for the cycle 2 corrector step is

$$
\frac{2\rho_i^{n+1}\left(u_i^{n+1,k+1} - u_i^{*n+1}\right)}{\Delta t} = \frac{1}{6}\left[\frac{\sigma_t}{c}\left(F_r - \frac{4}{3}E_r u\right)\right]_i^n + \frac{1}{6}\left[\frac{\sigma_t}{c}\left(F_r - \frac{4}{3}E_r u\right)\right]_i^{n+1/2}
$$
$$
+ \frac{2}{3}\left[\frac{\sigma_t}{c}\left(F_r - \frac{4}{3}E_r u\right)\right]_i^{n+1,k} ,
$$
(A.8)

where the $*$ terms come from the MHM corrector stage. The cell-averaged terms on the right hand side are are computed by taking the linear average of the corresponding expressions evaluated at the interior edges, e.g.,

$$
\left[\frac{\sigma_t}{c}\left(F_r - \frac{4}{3}E_r u\right)\right]_i = \frac{1}{2}\left[\frac{\sigma_{t,i,L}}{c}\left(F_{ri,L} - \frac{4}{3}E_{ri,L}u_{i,L}\right)\right]
$$
$$
+ \frac{1}{2}\left[\frac{\sigma_{t,i,R}}{c}\left(F_{ri,R} - \frac{4}{3}E_{ri,R}u_{i,R}\right)\right] . \quad (A.9)
$$

It is noted that in the absence of an extraneous momentum source, $\rho^{*n+1} = \rho^{n+1}$. In the presence of MMS sources, ρ is updated prior to entering the iteration loops. The Crank-Nicolson discretization of the velocity update equation for the Cycle 1 corrector is

$$
\frac{2\rho_i^{n+1/2}\left(u_i^{n+1/2,k+1} - u_i^{*n+1/2}\right)}{\Delta t} = \frac{1}{2}\left[\frac{\sigma_t}{c}\left(F_r - \frac{4}{3}E_r u\right)\right]_i^n + \frac{1}{2}\left[\frac{\sigma_t}{c}\left(F_r - \frac{4}{3}E_r u\right)\right]_i^{n+1/2,k} .
$$
(A.10)

The Backward-Euler discretization of the velocity update for the predictor stages are analogously defined.

Appendix A.3.2. Radiation and Material Energy Equations

The radiation and material energy equations must be linearized to be solved. We use a standard Newton linearization, with temperature dependent material properties lagged one iteration [24]. Upon linearization, the

radiation unknowns can be directly determined, followed by solution for new internal energies. The linearization process is tedious but straightforward. For brevity, we provide the non-linear equations here.

With the updated momentum, a kinetic energy can be defined, allowing for new internal energies to be obtained. However, to simultaneously solve the radiation and material energy balance equations, hydrodynamic quantities need to be evaluated at cell edges. The slopes Δ_i evaluated during the predictor step of the cycle, as given in Eq. (A.3), are used to extrapolate edge quantities during that cycle. Evaluation of edge densities is achieved by applying the slopes as given by Eq. (A.5):

$$\rho_{i,L}^k = \rho_i^k - \frac{\Delta \rho_i^n}{2} \,. \tag{A.11}$$

Evaluation of edge velocities is achieved based on ρ and ρu at edges, e.g.,

$$u_{i,L}^k = \frac{(\rho u)_{i,L}^k}{\rho_{i,L}^k} = \frac{(\rho u)_i^k - \frac{\Delta (\rho u)_i^n}{2}}{\rho_i^k - \frac{\Delta \rho_i^n}{2}} \,. \tag{A.12}$$

As explained in Section Appendix A.4, internal energy unknowns, and thus material temperature, use slopes that are independent of the MUSCL-Hancock slopes. This modifies the E^* terms within a cycle. These radiation internal energy slopes are denoted by δe. Evaluation of edge internal energies is thus performed as follows:

$$e_{i,L}^k = e_i^k - \frac{\delta e_i^n}{2} \,. \tag{A.13}$$

These internal energy slopes are only updated at the end of each stage, i.e., when the nonlinear iteration for the corrector step have been converged.

With hydrodynamic variables defined, discretized equations for the radiation and material energy balance equations can be defined. A lumped linear discontinuous (LLDG) spatial discretization is employed for the S_2 equations [?]. The lumping of the equations is strongly resistant to negative solutions in 1D [?]. Standard upwinding is used to define true face intensities in terms of interior-edge intensities that define the linear dependence of the intensity within a cell. For reference, the radiation equation for the positive direction of flow, the left interior-edge unknown, and the first

Backward-Euler stage is

$$
\frac{4}{c}\frac{\psi_{i,L}^{+,n+1/4,k+1} - \psi_{i,L}^{+,n}}{\Delta t} = -\frac{2\mu^+}{h_i}\left(\psi_i^{+,n+\frac{1}{4},k+1} - \psi_{R,i-1}^{+,n+\frac{1}{4},k+1}\right) - \frac{1}{2}\sigma_{t,i,L}^k\psi_{i,L}^{+,k+1}
$$
$$
+ \frac{\sigma_{s,i,L}^k}{2}\phi_{i,L}^{n+\frac{1}{4},k+1} + \frac{1}{2}\sigma_a ac\left(T_{i,L}^{n+1/4,k+1}\right)^4 .
$$
(A.14)

where $\psi_i^+ = (\psi_{i,L}^+ + \psi_{i,R}^+)/2$. The corresponding equation for the right unknown is

$$
\frac{4}{c}\frac{\psi_{i,R}^{+,n+1/4,k+1} - \psi_{i,R}^{+,n}}{\Delta t} = -\frac{2\mu^+}{h_i}\left(\psi_{i,R}^{+,n+\frac{1}{4},k+1} - \psi_i^{+,n+\frac{1}{4},k+1}\right) - \frac{1}{2}\sigma_{t,i,R}^k\psi_{i,R}^{+,k+1}
$$
$$
+ \frac{\sigma_{s,i,L}^k}{2}\phi_{i,R}^{n+\frac{1}{4},k+1} + \frac{1}{2}\sigma_a ac\left(T_{i,R}^{n+1/4,k+1}\right)^4 .
$$
(A.15)

For 1D, the S_2 equations can be directly solved efficiently.

The material energy balance equations are also discretized in space to determine new edge values. The Crank-Nicolson discretization of the material energy balance equation for the L unknowns is

$$
\frac{E_{i,L}^{n+1/2,k+1} - E_{i,L}^{*n+1/2}}{\Delta t} = -\frac{1}{2}\left[\sigma_a c\left(aT^4 - E_r\right)\right]_{i,L}^n - \frac{1}{2}\sigma_{a,i,L}^k c\left[aT^4 - E_r\right]_{i,L}^{n+1/2,k+1}
$$
$$
+ \frac{1}{2}\left[\sigma_t\frac{u}{c}\left(F_r - \frac{4}{3}E_r u\right)\right]_{i,L}^n + \frac{1}{2}\left[\sigma_t\frac{u}{c}\left(F_r - \frac{4}{3}E_r u\right)\right]_{i,L}^{n+1/2,k} .
$$
(A.16)

The BDF2 discretization of the energy update equation is

$$
\frac{E_{i,L}^{n+1,k+1} - E_{i,L}^{*n+1}}{\Delta t} = -\frac{1}{6}\left[\sigma_a c\left(aT^4 - E_r\right)\right]_{i,L}^n - \frac{1}{6}\left[\sigma_a c\left(aT^4 - E_r\right)\right]_{i,L}^{n+1/2}
$$
$$
- \frac{2}{3}\sigma_{a,i,L}^k c\left[aT^4 - E_r\right]_{i,L}^{n+1,k+1} + \frac{1}{6}\left[\sigma_t\frac{u}{c}\left(F_r - \frac{4}{3}E_r u\right)\right]_{i,L}^n
$$
$$
+ \frac{1}{6}\left[\sigma_t\frac{u}{c}\left(F_r - \frac{4}{3}E_r u\right)\right]_{i,L}^{n+1/2} + \frac{2}{3}\left[\sigma_t\frac{u}{c}\left(F_r - \frac{4}{3}E_r u\right)\right]_{i,L}^{n+1,k} .
$$
(A.17)

22

To conserve total energy, the newly estimated edge total material energies, $E_{L,i}^{k+1}$ and $E_{R,i}^{k+1}$, are averaged to compute new cell-averaged total energies E_i^{k+1}; no modifications are made to the hydrodynamic slopes Δ_i. Averaging the total energy in this manner produces an unavoidable discrepancy between cell-averaged and edge internal energies.

Appendix A.4. Using Radiation Internal Energy Slopes

As discussed in the introduction, the radiation solver and hydro solver use different internal energy slopes as an approach to preserve the equilibrium diffusion limit. The implementation of separate slopes is a proof of concept for higher dimensions. To mitigate confusion, in this section we will denote the hydro-state internal energy variables as e and the internal energy variables coming from the non-linear radiation solves as e^r. Care must be taken to ensure that total energy is conserved. The modified slopes are only applied to the implicit terms in each nonlinear solve.

During the MHM solve, we use the standard slope reconstruction formulas to advect variables to state U^* (or U^{**}), including total energy E. Then, in the non-linear iteration loop for the radiation and internal energy densities we use a modified slope for E^*, denoted ΔE^{r*}, that will preserve the diffusion limit. This ΔE^{r*} is based on the edge values of e^r of *the last iteration of the previous nonlinear radiation solve.* For example, if we are solving the cycle 1 corrector from state e^* to $e^{n+1/2}$, we use the edge values of e^r from the last iteration of the solve for $e^{r,n+1/4}$ to construct the slopes for $\Delta E^{r,*}$. The value of $\Delta E^{r,*}$ does not change over the duration of the nonlinear solve.

Slopes $\Delta^{n+\frac{1}{2}}$ and $\delta e^{n+\frac{3}{4}}$ are again used to evaluate edge quantities. At the end of the cycle, the new internal energy slopes δe^{n+1} are saved for the next cycle.

For the nonlinear solve we need the to use δe^r to construct ΔE^{*r} in the next solve (and thus the values $E_{R/L}^* = E_i^* \pm \frac{1}{2}\Delta E^{r*}$ needed for the LD radiation solve). We approximate this slope based on the hydro values for E^* as:

$$\Delta E^{r*} = E_R^{r*} - E_L^{r*} \tag{A.18}$$

where

$$E_R^{r*} = \rho_R^* \left((u_R^*)^2 + e_i^* + \delta e^{r,n+1/4}\right), \tag{A.19}$$

$$E_L^{r*} = \rho_R^* \left((u_L^*)^2 + e_i^* - \delta e^{r,n+1/4}\right), \tag{A.20}$$

and subscript i denotes cell average quantities. The edge values of ρ and u are evaluated using the MHM slopes as usual. Once we have completed

23

the nonlinear solve for $e_{L/R}^{r,n+1/2}$, we must compute the change made to the cell-averaged total energy for the next MHM solve, such that total energy is conserved. The formula for the new total energy is

$$E_i^{n+1/2} = \frac{1}{2} \left[\rho_L \left(\frac{1}{2} u_L^2 + e_L^r \right) + \rho_R \left(\frac{1}{2} u_R^2 + e_R^r \right) \right]^{n+1/2} \tag{A.21}$$

where all variables are at time $t^{n+1/2}$. The internal energy slopes are computed and stored for the next nonlinear solve. For the first solve, the internal energy slopes are assumed zero.
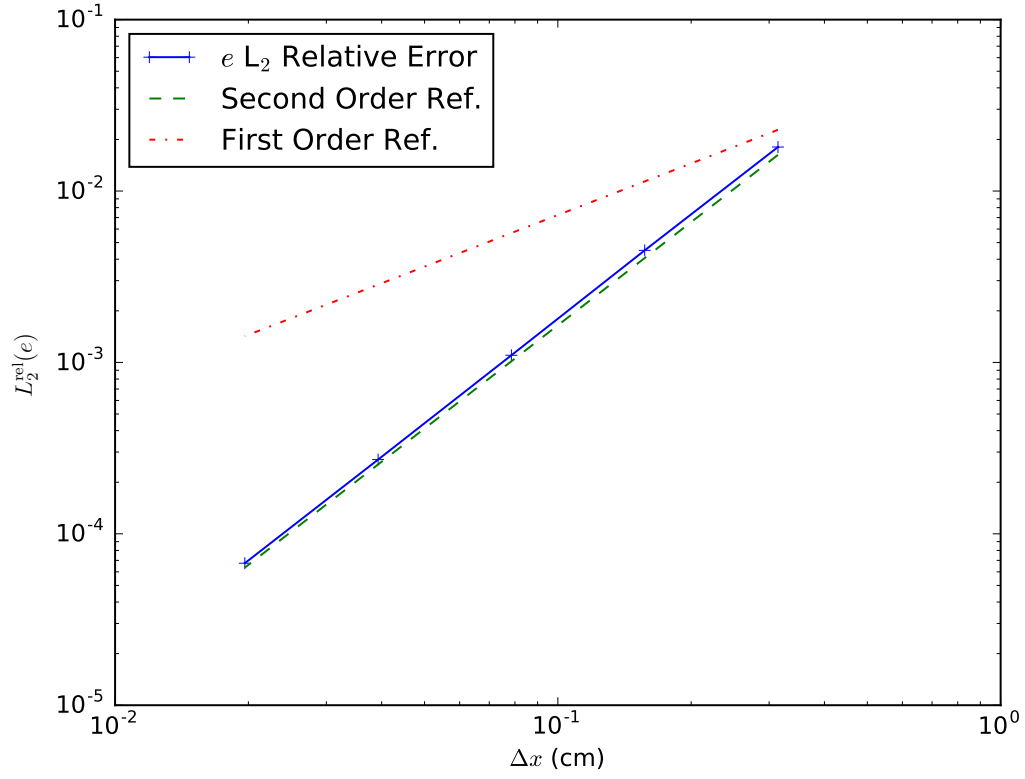
Figure A.1: Convergence in space of internal energy e for the equilibrium diffusion limit MMS problem
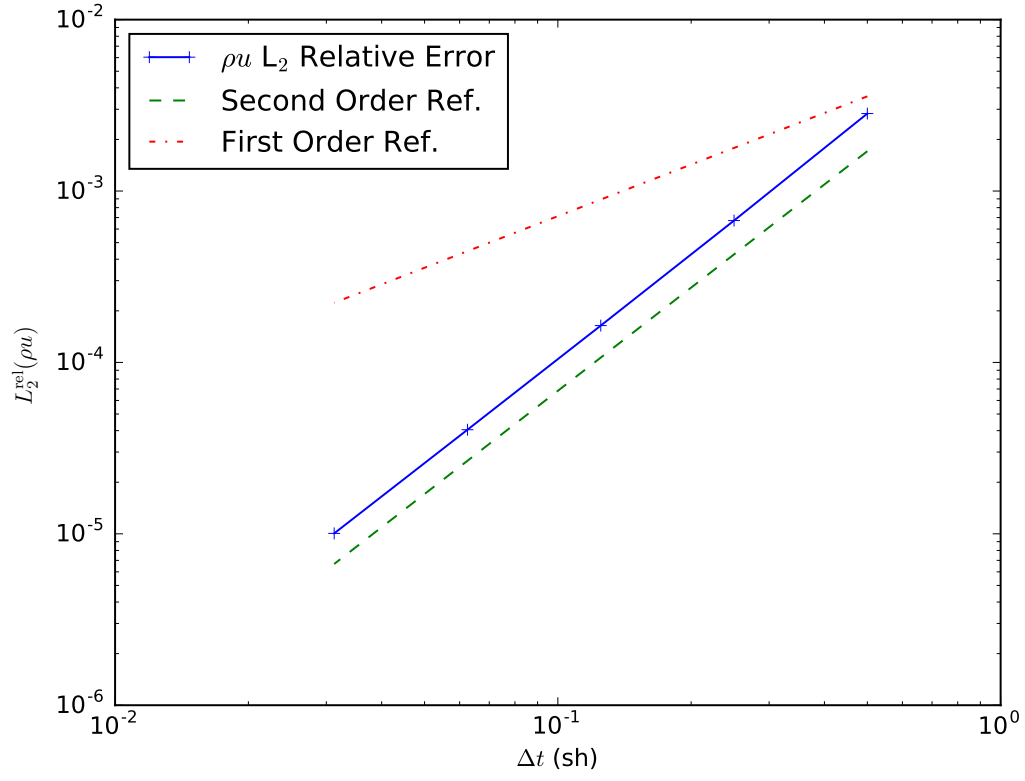
Figure A.2: Convergence in time of momentum ρu for the equilibrium diffusion limit MMS problem
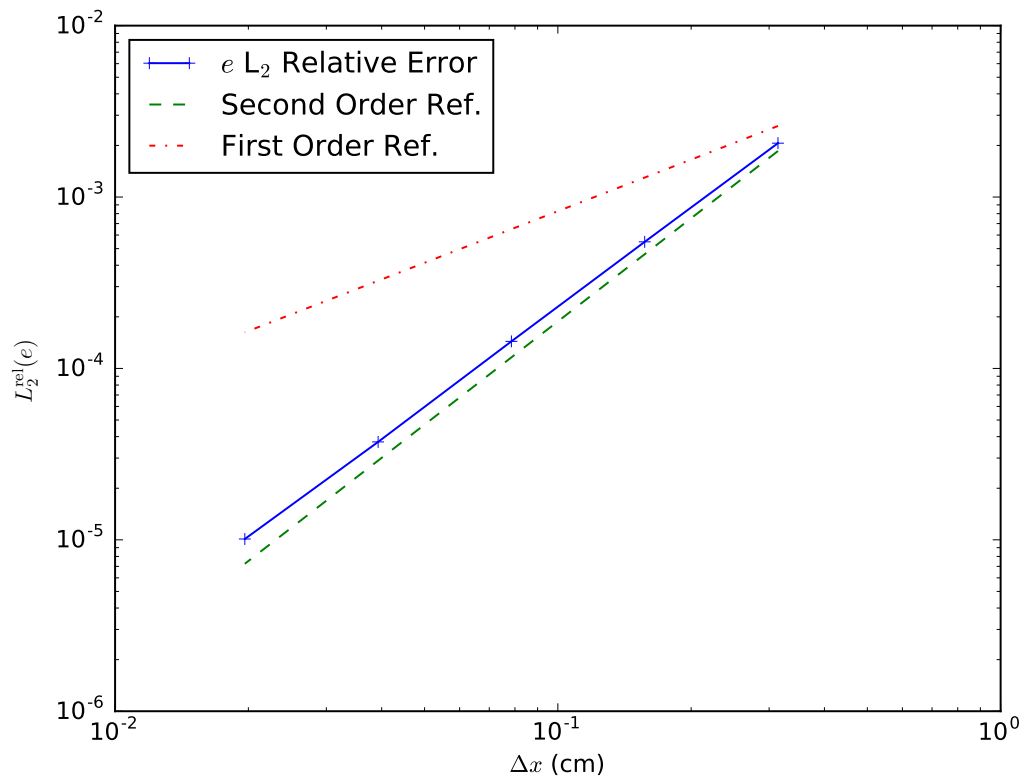
Figure A.3: Convergence in space of internal energy e for the MMS streaming problem
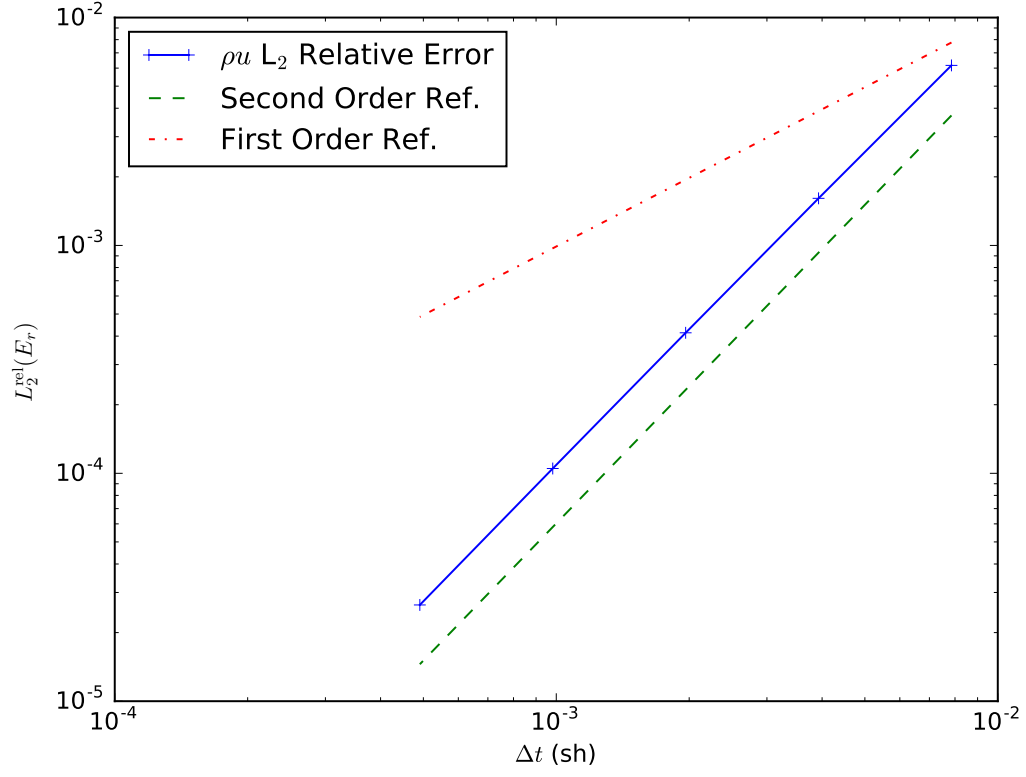
Figure A.4: Convergence in time of radiation energy density E_r for the MMS streaming problem
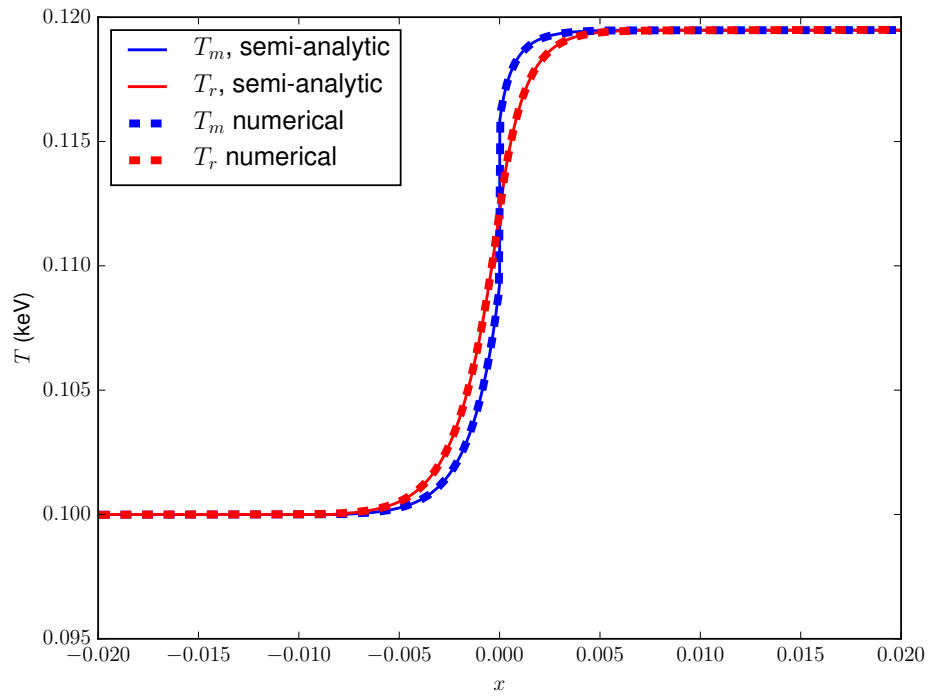
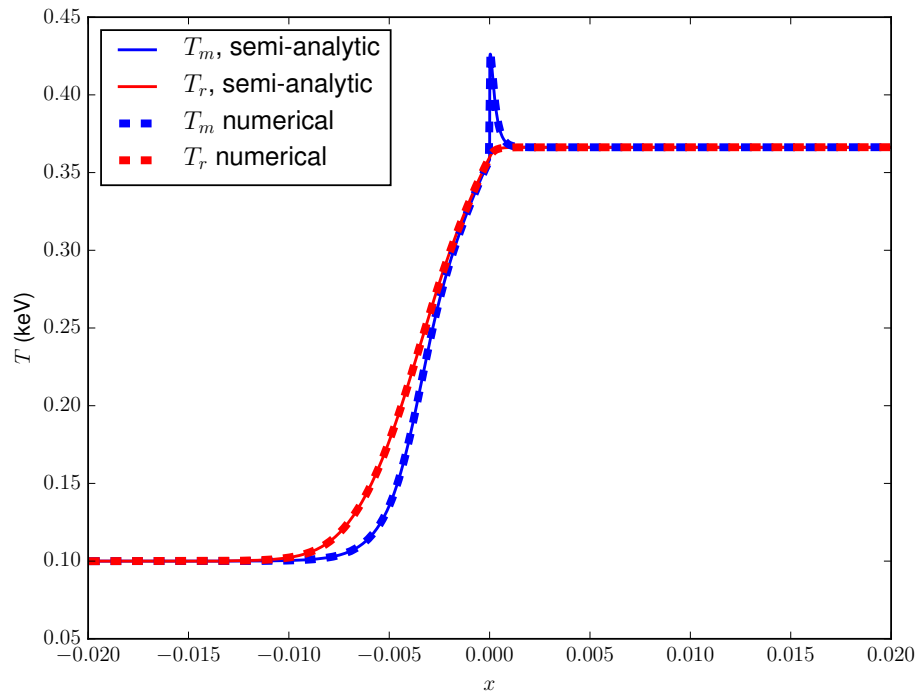Figure A.5: **Mach 1.2 radiative shock fluid and radiation temperatures.**

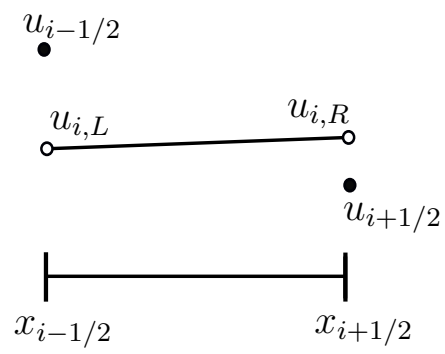Figure A.6: **Mach 3.0 radiative shock fluid and radiation temperatures.**

Figure A.7: Illustration of face and interior unknowns.

Table A.1: Initial condition values for the Mach 1.2 radiative shock problem

Parameter	Pre-shock Value	Post-shock Value	Units
ρ	1.00000000e+00	1.29731782e+00	g cm^{-3}
u	1.52172533e-01	1.17297805e-01	cm sh^{-1}
T	1.00000000e-01	1.19475741e-01	keV
E	2.60510396e-02	3.13573034e-02	Jks cm^{-3}
E_r	1.37201720e-06	2.79562228e-06	Jks cm^{-3}
F_r	0.00000000e+00	0.00000000e+00	Jks cm^{-2} s^{-1}

Table A.2: Initial condition values for the Mach 3 radiative shock problem

Parameter	Pre-shock Value	Post-shock Value	Units
ρ	1.00000000e+00	3.00185103e+00	g cm^{-3}
u	3.80431331e-01	1.26732249e-01	cm sh^{-1}
T	1.00000000e-01	3.66260705e-01	keV
E	8.68367987e-02	1.83229115e-01	Jks cm^{-3}
E_r	1.37201720e-06	2.46899872e-04	Jks cm^{-3}
F_r	0.00000000e+00	0.00000000e+00	Jks cm^{-2} s^{-1}